AIAA JOURNAL
Vol. 48, No. 10, October 2010

Simultaneous Particle Image Velocimetry and Microphone Array Measurements on a Rod-Airfoil Configuration

A. Henning*
Berlin Institute of Technology, 10587 Berlin, Germany
and
L. Koop† and K. Ehrenfried†
DLR, German Aerospace Center, 37073 Göttingen, Germany

DOI: 10.2514/1.J050314

The aeroacoustic sound generation process on a rod-airfoil configuration has been investigated by means of simultaneous particle image velocimetry in the near field and phased-microphone-array measurements in the far field. Up to 20,000 particle image velocimetry snapshots per field of view have been recorded. A coplanar multiplane particle image velocimetry system has been used, providing statistically independent samples of the temporal derivative of the velocity field. Both measurements were conducted in a synchronized manner so as to enable the calculation of the cross-correlation between the acoustic pressure and flow quantities derived from the measured velocity fluctuations. The main idea of the concept used in the study presented here was to use the coefficient matrix obtained from the aforementioned correlation to identify regularities in the near-field fluctuations that are related to the radiated sound field. Additionally, a technique to localize flow structures responsible for the far-field sound by means of the calculation of the near-field intensity has been tested.

Nomenclature

c	=	chord length
c_0	=	speed of sound
d	=	cylinder diameter
f	=	frequency
f_s	=	sampling frequency
$\mathbf{I}$	=	intensity
N	=	number of snapshots by particle image velocimetry
n	=	index of particle image velocimetry snapshot
p	=	sound pressure
Re	=	Reynolds number
s	=	airfoil span
t	=	time
U, V	=	time-averaged velocity components
U_∞	=	freestream velocity
u, v	=	velocity components with respect to x and y
x, y	=	Cartesian coordinates of the particle image velocimetry plane
σ	=	root-mean-square value
τ	=	time difference
ϕ	=	acoustic variable
ψ	=	flow quantity
ω_z	=	out-of-plane vorticity
$\langle\cdot\rangle$	=	ensemble average

I. Introduction

A TURBULENT flowfield, described by the Navier–Stokes equation, can result in pressure fluctuations even outside of this flowfield where the medium is on average at rest. One major objective in aeroacoustic research is the identification of those flow structures that are involved in the generation mechanisms of aeroacoustic noise sources. Lighthill [1] rearranged the terms in the basic equations of fluid motion in such a way that the left-hand side becomes a wave equation. The resulting Lighthill equation exactly describes the flowfield and the generated far-field pressure fluctuations without loss of generality. But it is difficult to predict the exact proportion of the turbulent kinetic energy that is radiated as sound, since usually only a very small fraction of the complete energy is transferred into the far-field pressure fluctuations [1]. Common approaches for the prediction of the acoustic far field from the near-field data are mostly based on an acoustic analogy, where the source strength is determined by experiments or numerical simulations. In this way it is possible to estimate how much noise is generated in a certain flowfield. Lorenzoni et al. [2] calculated the far-field noise based on time-resolved particle image velocimetry (PIV) measurements for a rod-airfoil configuration similar to the one used in here. But several things have to be kept in mind in order to obtain an accurate far-field prediction. Typically in aeroacoustics a large amount of the source strength cancels itself out so that only a relative small portion radiates to the far field. To predict this destructive interference correctly, the sources have to be determined with a certain amount of accuracy and in the complete source domain. Especially cutoff errors, where a certain part of the source distribution is missing, can lead to huge errors in the far-field prediction [3]. Another point to remember is that the far-field prediction does not necessarily give a deep insight into the source process itself. Often, even the simple question of where the sound comes from cannot be unequivocally answered. Commonly, the accuracy of a PIV measurement is estimated to be of the order of 0.1 pixels [4]. Even if this value can be decreased by one order of magnitude by means of advanced PIV evaluation algorithms [5], this still results in an accuracy for the investigation presented here of not better than 0.1% (see Sec. IV.A). Gradients derived from such PIV measurements will have an even lower accuracy than the velocity data itself [6], so that it would be overly ambitious to attempt to calculate acoustic source terms directly from the acquired instantaneous velocity field. The goal in the present study is to calculate time-averaged rather than instantaneous quantities, where, for the ideal case, random errors should be reduced by increasing the number of samples N. But even then, the required accuracy is hard to achieve, since the error in the estimated moments decreases with $\sqrt{N}$ only and the archivable accuracy is limited by the filter effect and noise of the PIV process chain. One way around this is the simultaneous measurement of the acoustic pressure in the far field together with

Presented as Paper 2009-3184 at the 15th AIAA/CEAS Aeroacoustics Conference, Miami, FL, 11–13 May 2009; received 9 November 2009; revision received 20 May 2010; accepted for publication 30 May 2010.

*Research Scientist, Department of Astronautics and Aeronautics, Marchstrasse 12-14.

†Research Scientist, Institute of Aerodynamics and Flow Technology, Bunsenstrasse 10.

some other near-field quantity. In this manner the far-field pressure can be correlated with the near-field quantity to identify flow structures that are subject to the same physical phenomenon as the aeroacoustic sources in a statistical manner.

The simultaneous measurement of acoustic pressure fluctuations in the far field together with some near-field quantity has been investigated by various authors in the past [7–9]. Previous experiments [10] have shown that synchronized PIV and microphone measurements can be used to obtain the cross-correlation function between a near-field quantity and the acoustic pressure in the far field. The authors have shown that for the case of a relatively simple flow configuration (e.g., cylinder wake flow) a reasonable amount of 5000 PIV recordings are sufficient to obtain a significant correlation between the velocity fluctuations and the far-field pressure in the whole region of interest (ROI) measured via PIV. This was not the case for a more complex configuration (e.g., a slat flowfield of a swept wing), probably because of the more three-dimensional character of this flowfield compared to the cylinder wake flowfield. The studies summarized in [10] have been performed in a closed-test-section wind tunnel that has not been optimized for acoustic measurements. Furthermore, the sound field has been recorded by only one inflow microphone. In the present study, measurements are conducted in an aeroacoustic wind tunnel with an open test section in an anechoic chamber. The acoustic data were acquired using a microphone array consisting of 87 microphones. Furthermore, a coplanar multiplane PIV system was used. As opposed to continuously-time-resolved measurement techniques (e.g., hot-wire, high-speed PIV), it provides statistically independent samples of the temporal derivatives derived from the velocity field. This is an important feature if statistical quantities in flow configurations with large coherent structures are to be calculated.

A rod-airfoil configuration is examined by means of the described correlation method. It is similar to the AIAA/CEAS Benchmark configuration described in [11] and several experimental and numerical results are available for comparison [11–13]. In such a configuration the airfoil undergoes a broadband perturbation dominated by the turbulent periodic shedding frequency of the vortex street behind the rod. Compared to the flowfield generated by a single cylinder, the radiated noise is spread over a wider range of frequencies. The theoretical background, including the adopted acoustic analogy, is given in the following section. The experimental setup, the data processing, and the results are presented in Secs. III, IV, and V, respectively.

II. Theoretical Background

A. Intensity Calculations

An approach based on the intensity analysis will be described in the following. First, the analysis requires a conservation principle for acoustic or fluctuation energy. To obtain an appropriate conservation principle it is possible to consider an acoustic analogy (for example, the acoustic analogy of Lighthill):

$$\frac{\partial^2 \rho'}{\partial t^2} - c_0^2 \Delta \rho' = \frac{\partial^2}{\partial x_i \partial x_j} T_{ij}$$

where T_{ij} denotes the Lighthill stress tensor, or the equation of Howe

$$\partial^2 B/\partial t^2 - c_0^2 \Delta B = \nabla \cdot (\omega \times \mathbf{v})$$

which holds in the low-Mach-number limit and has the stagnation enthalpy B as acoustic variable. Both analogies are inhomogeneous wave equations of the form

$$\partial^2 \phi/\partial t^2 - c_0^2 \Delta \phi = q$$

The wave operator on the left-hand side describes the acoustic propagation of fluctuations in a medium at rest. Hence, the right-hand side can be regarded as sources in a medium at rest, generating the equivalent density or stagnation-enthalpy fluctuations of the flowfield. It is important for the present study that the wave operator is self adjoint and that therefore a conservation principle for fluctuation energy exists. In the case of the present wave operator this can be written as

$$\partial e/\partial t + \nabla \cdot \mathbf{I} = q_e$$

where the specific fluctuation energy e is given by

$$e = \frac{1}{2}(\dot{\phi})^2 + \frac{c_0^2}{2}(\operatorname{grad} \phi)^2$$

and the intensity vector $\mathbf{I}$ is

$$\mathbf{I} = -c_0^2 \dot{\phi} \operatorname{grad} \phi \tag{1}$$

The energy principle can be derived using a Lagrangian analysis. Möhring [14] shows that for an acoustic analogy with a more complicated wave operator and expressions for e and $\mathbf{I}$. However, the given energy e and intensity $\mathbf{I}$ do not correspond to the energy and intensity expression commonly used in acoustics. Only if ϕ is the acoustic potential, $\mathbf{I}$ formally corresponds to the standard acoustic intensity $p'\mathbf{v}'$ up to a constant factor. In general, the given expression for e defines an energy in the sense that it is a nonnegative quantity with square dependence on the fluctuation variable, which indicates the specific strength of the fluctuations. In the following, e and $\mathbf{I}$ are called fluctuation energy and intensity, respectively. In principle, it is always possible to introduce a constant with the appropriate physical unit in the definitions of e and $\mathbf{I}$, so that $\mathbf{I}$ has the physical unit of Watt per square meter. But this is not necessary if only the spatial distribution and not the absolute value of the intensity and fluctuation energy is of interest. The quantity q_e on the right-hand side can be considered as the local production rate of fluctuation energy. In the far field where the flow is at rest, this quantity vanishes. In the near field the value of q_e indicates the presence of a source of the fluctuations. But a negative production rate and reactive power is also possible. To analyze the source efficiency, the time-averaged intensity field is considered. One has the relation

$$\nabla \cdot \langle \mathbf{I} \rangle = \langle q_e \rangle$$

where the angle brackets indicate the temporal average. Hence, the quantity $\nabla \cdot \langle \mathbf{I} \rangle$ can be used as a measure for the local source efficiency. It is clear that the resulting source efficiency depends on the selected acoustic analogy. If the density fluctuation ρ' is taken as variable ϕ the distribution of $\nabla \cdot \langle \mathbf{I} \rangle$ is most probably different from the result that is obtained for the stagnation enthalpy B. But this deviation of source efficiency reflects the difference in the source distribution between both acoustic analogies. Of course, not all generated ρ of B fluctuations are radiated as sound to the far field. It is also possible that fluctuations are effectively generated in the near field that do not belong to acoustic waves at all. For example, the generation of a vortex street involves the production of entropy and density fluctuations. These entropy and density fluctuations are convected in the flow. The field $\langle \mathbf{I} \rangle$ would contain the corresponding fluctuation transport by convection as well. The present study is based on flowfield measurements in the near field and acoustic pressure measurements in the far field outside the open jet where the medium is at rest. However, the intensity analysis has to be based on a quantity that can be calculated from the measured values. Therefore, the inhomogeneous wave equation

$$\frac{\partial^2 v}{\partial t^2} - c_0^2 \Delta v = q$$

is considered here with one velocity component $\phi = v$ as a fluctuation variable. It is clear that $\phi = v$ fulfills the homogeneous wave equation in the region where the medium is at rest. There the right-hand side q is small in an acoustic sense. In the near field the quantity q represents the sources of the v fluctuations. In principle, the inhomogeneous wave equation for $\phi = v$ can be considered as an acoustic analogy. The analogies of Lighthill and Howe given above are obtained by an recast of the fundamental equations of fluid motion, so that an expression for the source strength q exists. But this is not required for the present intensity analysis at all. Only the

existence of the source strength q and its spatial containment to the near field is important. Then it is reasonable to take the fluctuations of the quantity $\phi = v$ for an intensity analysis. The quantity $\nabla \cdot \langle \mathbf{I} \rangle$ then indicates where v fluctuations are effectively generated in the near field. Here, a case is considered in which most of the velocity fluctuations in the near field are related to convective transport of vortical structures. This means that the intensity is dominated by convective effects and that the intensity contribution from the acoustic waves may be miniscule compared to the overall value. Therefore, it may not be possible to obtain the acoustic intensity contribution from the experimental data. But the idea is that, at least in the vicinity of the source region, the reactive power (which is involved with the source process) becomes observable.

B. Cross-Correlation Coefficient

The sample correlation coefficient $R_{\psi,p}(\mathbf{x}, \tau)$ will be defined as

$$R_{\psi,p}(\mathbf{x}, \tau) = \frac{S_{\psi,p}(\mathbf{x}, \tau)}{\sigma_\psi(\mathbf{x})\sigma_p} = \frac{\langle \psi'(\mathbf{x}, t) p'(t + \tau) \rangle}{\sqrt{\langle \psi'(\mathbf{x}, t)^2 \rangle \langle p'(t)^2 \rangle}} \tag{2}$$

where $\psi'(\mathbf{x}, t)$ represents the zero-mean part of a near-field quantity ψ measured at position $\mathbf{x}$ and time t. The variable τ is the time shift between the pressure signal and ψ. The correlation coefficient is normalized by the root-mean-square (rms) values of ψ' and p', which are denoted by $\sigma_\psi(\mathbf{x})$ and σ_p. In the present experiments two discrete time series are considered: A near-field quantity derived from the flowfield (which is recorded by the PIV system at discrete times t_n) and the far-field pressure (which is recorded at discrete times $t_n + m\Delta\tau$) simultaneously with the PIV measurements. The cross-correlation function $S_{\psi,p}(\mathbf{x}, \tau)$ between the near-field quantity and the acoustic pressure can be estimated in a discrete manner using

$$S_{\psi,p}(\mathbf{x}, \tau) = \frac{1}{N} \sum_{n=1}^{N} [\psi'(\mathbf{x}, t_n) p'(t_n + m\Delta\tau)] \tag{3}$$

where $\tau = \tau(m) = m\Delta\tau$. The rms value for the zero mean part of the near-field quantity, which is required for normalization, is calculated from the measured data by

$$\sigma_\psi(\mathbf{x}) = \sqrt{\frac{1}{N} \sum_{n=1}^{N} \psi'(\mathbf{x}, t_n)^2} \tag{4}$$

In an analogous manner, the standard deviation σ_p of the acoustic pressure is computed, except that there the averaging is carried out over all recorded pressure samples. It should be noted that in the result Sec. V.C, a delayed and summed-up pressure signal from a number of microphones is used. Therefore, for the correlation results presented here, τ correspond to a retarded time at which the sound travel time from a chosen point to the microphones is approximately compensated.

Following Howe [15] the aeroacoustic source strength can be expressed using the Lamb vector $\boldsymbol{\omega} \times \mathbf{v}$, where $\boldsymbol{\omega} = \operatorname{curl} \mathbf{v}$ denotes the vorticity. Previous results have show that in the low-Mach-number limit the cross-correlation between $\boldsymbol{\omega} \times \mathbf{v}$ and p is a reasonable starting point for an indication of which processes in the near field are responsible for the main part of the radiated sound [10]. After splitting the vorticity and the velocity into mean and fluctuating parts and rearranging the correlations to be calculated are $\langle \mathbf{v}' p' \rangle$, $\langle \boldsymbol{\omega}' p' \rangle$ and $\langle (\boldsymbol{\omega}' \times \mathbf{v}')_i p' \rangle$ [10]. With the 2-D PIV method used in the present study the in-plane components of the correlation $\langle \mathbf{v}' p' \rangle$ and the out-of-plane component of $\langle \boldsymbol{\omega}' p' \rangle$ can be calculated only. But the cross-correlation with fluctuations $\mathbf{v}'$ and $\boldsymbol{\omega}'$ can give an indication of which processes in the near field are responsible for the main part of the radiated sound.

III. Experimental Setup and Methods

A. Flow Configuration

Experiments were conducted in the Aeroacoustic Wind Tunnel Braunschweig of DLR, German Aerospace Center, which is an

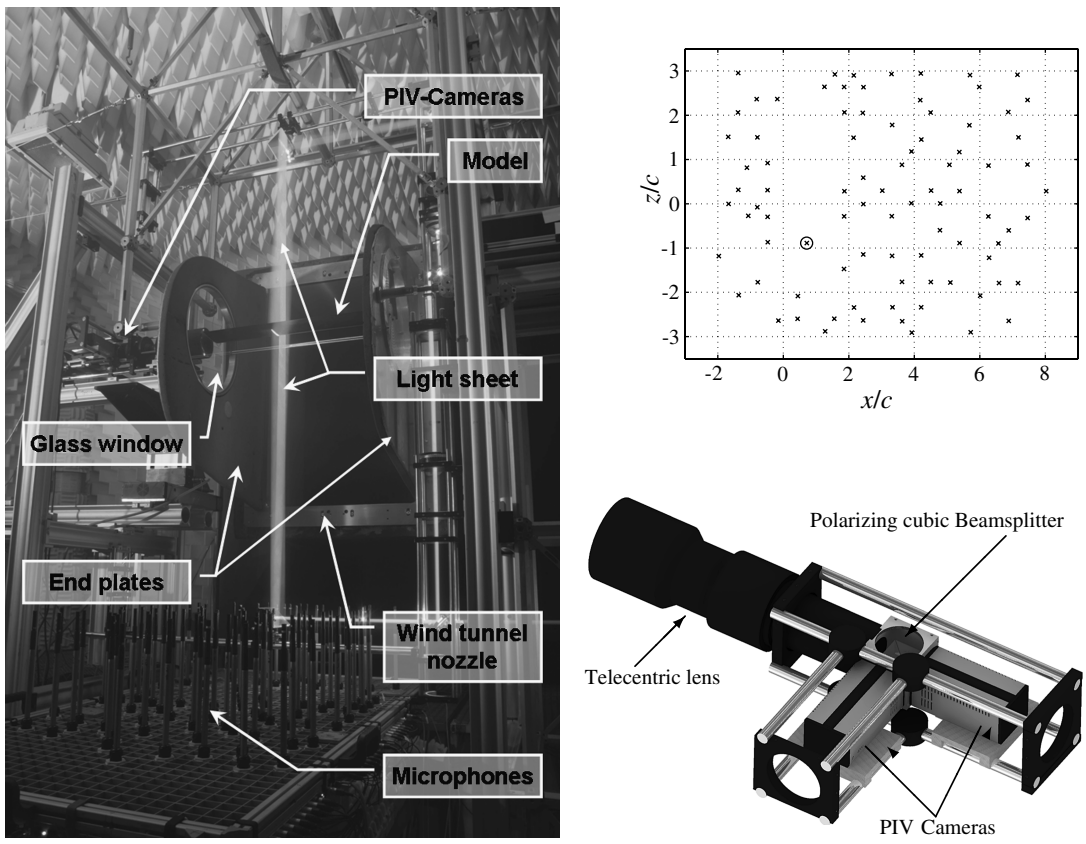

Fig. 1 Experimental setup (left); microphone positions $z/c = -8$ for all microphones, with reference microphone marked by a circle (right, top); and multiplane camera system (bottom).

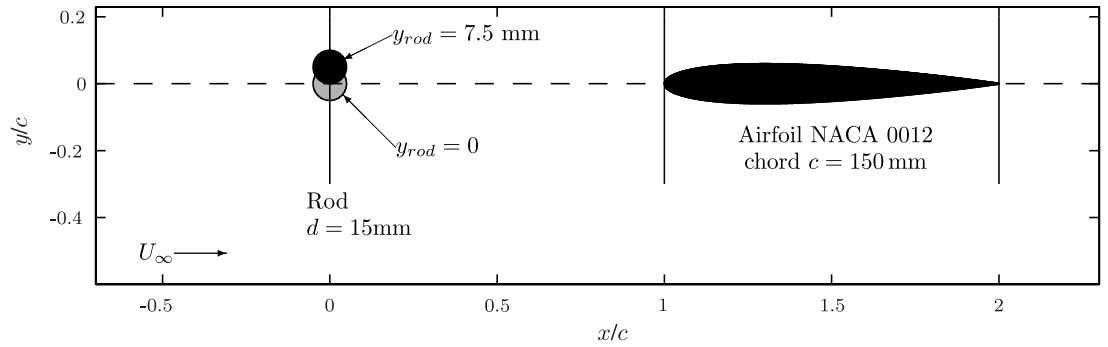

Fig. 2 Investigated rod-airfoil configuration. The span of the airfoil and the length of the cylinder is $l = 800$ mm.

open-jet closed-circuit anechoic test facility with a rectangular 0.8 by 1.2 m nozzle exit. Figure 1 (left) shows a picture of the experimental setup. Measurements have been performed at freestream velocities $U_\infty = 30$ m/s ($Re_c = 300,000$) and $U_\infty = 50$ m/s ($Re_c = 500,000$) on a rod-airfoil configuration. The measurement setup consists of a symmetric NACA-0012 airfoil (chord $c = 150$ mm) located one chord downstream of a rod ($d/c = 0.1$). They are installed between end plates that are mounted at two opposing sides of the wind-tunnel nozzle. The rod-airfoil arrangement and coordinates are illustrated in Fig. 2. The span of the configuration is $s = 800$ mm. Both the rod and the airfoil are mounted on two turnable concentric aluminum disks, installed in-plane with the end plates. The rod is fixed to the disks, whereas the airfoil can be turned around the center of the disks, allowing both bodies to turn independently around a common axis. To obtain optical access for the PIV recordings, one of the disks has an insertion made out of borosilicate glass. The configuration is similar to the one described by Jacob et al. [11].

B. PIV Measurements

Velocity data are acquired with a two-dimensional, two component multiplane PIV system, capable to capture two components of the velocity vectors in a plane. The system consists of two independent double-pulse laser systems generating two coplanar light sheets, with the polarizations being perpendicular to each other. A polarizing beam splitter is installed between a telecentric camera lens (S5LPJ1555 by SILL) and two cameras (PCO, 4000) recording the light scattered by the tracer particles. Thus, the first and the second camera receive only light from the first and the second laser system, respectively. This setup allows the calculation of temporal velocity derivatives, since it can capture the velocity field at two successive time steps. Temporal derivatives are available for the ROI A and B. For all other regions of interest, the time delay between the two PIV double frames is set to 0.4 s in order to double the amount of statistically independent velocity samples. The frequency-doubled lasers (Q-switched Nd:YAG; Quantel CFR 200) emit laser pulses with a maximum energy of 200 mJ. They are operating at a repetition rate of 10 Hz. The charge-coupled-device cameras have a resolution of 4008×2672 pixels and a frame rate of 0.7 Hz, which therefore represents the sampling rate of the whole PIV setup. To avoid shadowing effects, the model is illuminated from the top and the bottom of the model simultaneously in the case of the ROI A. The telecentric lens (SILL S5LPJ1555) used in this setup has a magnification of 0.46 and a distortion of 0.1% at a fixed working distance of 320 mm. This results in a resolution of 51.2 px/mm for the used cameras. Any problems caused by particle images out of focus are avoided by use of the telecentric lens [16]. The Airy disc diameter of the particle images is of the order of 0.5 pixels [17]. But by a visual inspection of the recorded particle images, the image size is observed to be in the range of 2–3 pixels, which can probably be attributed to the lens aberrations and therewith the modulation transfer functions of the lens system used in the experiment [18]. The observed particle image diameter implies that the influence of undersampling remains below an rms bias of 0.01 pixels [19]. The flow is seeded with diethylhexylsebacate tracer particles with a mean particle diameter of approximately 1 μm [20]. The seeding is injected from a corner of the wind tunnel upstream of the rod-airfoil configuration in a way that the particles have to pass the complete wind tunnel before they reach the PIV field of view. Because of the strong velocity gradients the particles are undergoing while passing the driving fan, an increase of the mean particle diameter with time due to coagulation effects [20] is avoided [21]. Following Mei [22] the cutoff frequency for 1 μm particles is on the order of 15 kHz, based on a 50% energy response. In the cases of ROI A and B up to 20,000 pairs of images (snapshots) are analyzed per field of view. For all other regions of interest the number of snapshots is smaller (see Table 1). The PIV and the microphone measurements are performed in a synchronized manner. To avoid a jitter between the PIV timing and the far-field pressure data acquisition, both measurement systems are synchronized to a megahertz master clock. Figure 3 shows the cross-sectional view of the rod-airfoil model. The origin of the right-hand coordinate system is located in the midspan position of the cylinder axis when it is aligned with the airfoil chord at an angle of attack of $\alpha = 0°$. Two positions of the upstream cylinder have been investigated ($y_{\text{rod}}/c = 0$ and 0.05), as indicated in the sketch. The boxes indicate the regions of interest observed by the PIV camera system. Because of the limited working distance of the used telecentric lens, all ROI Are located at $z/c = 0.3$, a position slightly shifted from the midspan plane. In a first run this configuration is measured at both freestream velocities (30 and 50 m/s) at ROI A. For all subsequent measurements the freestream velocity is set to 50 m/s and the cylinder is shifted to $y_{\text{rod}}/c = 0.05$, in order to include an

Table 1 Summary of the measurement conditions for the different regions of interest

Run	ROI	U_∞, m/s	Samples	y_{rod}/c	$\partial v_i/\partial t$ available
1	A	30	20,000	0	Yes
2	A	30	15,000	+0.05	Yes
3	A	50	15,000	+0.05	Yes
4	B	50	12,000	+0.05	Yes
5	C	50	10,000	+0.05	——
6	D	50	10,000	+0.05	——
7	E	50	5,000	+0.05	——
8	F	50	5,000	+0.05	——

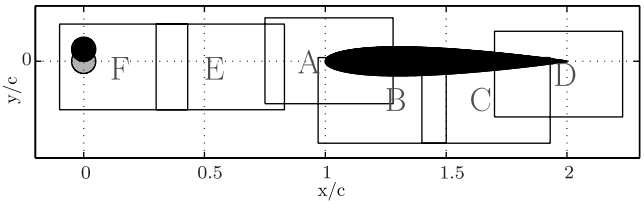

Fig. 3 Cross-sectional view of the rod-airfoil model with both positions of the rod ($y_{\text{rod}}/c = 0$ and 0.05). Boxes indicate the ROI observed by the PIV camera system.

almost turbulence free section in the lower region of the ROI B and C. The various configurations are listed in Table 1. Here, the results for the configurations with $U_\infty = 50$ m/s and $y_{\text{rod}}/c = 0.05$ are mainly presented.

C. Microphone Array

The microphone array consists of 87 microphones (M51 by LinearX) and is located outside the flowfield. The distance between the model and the microphone membranes is approximately 1.2 m. The microphone signals were simultaneously sampled with an A/D conversion of 16 bits at a sampling frequency of $f_s = 50$ kHz. All channels had an anti-aliasing filter at $f_u = 25$ kHz. The recording time for one measurement is $T = 3600$ s (1 h). To reduce the influence of low-frequency wind-tunnel noise on the measured signals a high-pass filter with a cutoff frequency $f_l = 500$ Hz has been applied. The exact position of the microphones is determined using an accurate phase calibration procedure described by Lauterbach et al. [23]. Figure 1 (right, top) depicts the measured positions of the microphones in the coordinate system of the rod-airfoil model. The far-field pressure fluctuations measured at the microphones are correlated with the near-field fluctuations obtained from PIV measurements as described in the next section.

IV. Data Processing

A. PIV Processing

The recorded particle image pairs are evaluated using an iterative multipass algorithm with window deformation. The method used here is similar to the one described by Nobach [24]. Rather then using a fixed number of evaluation passes, the iteration is repeated until it convergences to a *zero displacement*. If the iteration diverges or the estimated displacement is larger than a local threshold, the vector is treated as outlier. For the subpixel window shift an interpolation scheme based on a 11-point Gaussian filter kernel is used [19]. The cross-correlation of the interrogation-window (IW) pairs is calculated using the fast-Fourier-transform-based free-shape correlation [25]. The IW size is 64×64 px with an overlap of 50%. The number of skipped outliers is approximately 1% on average. Note that the histogram of the subpixel shift shows no bias of particle displacements toward integer pixel values (peak-locking) [26].

To calculate the temporal derivatives of the velocity field obtained by the multiplane PIV system described in Sec. III, the ROI recorded by the two cameras should match exactly. However, small changes in the angular orientation of the installed beam-splitter are causing relatively strong shifts of the image recorded by the second camera receiving the reflected light, making a sufficiently high accuracy for the overlap difficult to achieve. For the estimation of the translation and rotation between the two areas recorded by the cameras, a number of 1000 particle-image pairs is recorded with both cameras simultaneously at a low wind-tunnel speed of approximately $U_\infty = 5$ m/s. The rotation and translation between the image pairs is then calculated by means of the so-called ensemble correlation [27]. The therewith-obtained results are used to project the IW-pair coordinates defined for the first camera onto the image pairs captured by the second one.

Velocity vectors resulting from a PIV measurement are representing mean values over a specific volume and a specific time interval. The volume is defined by the thickness of the light sheet of 1 mm and the interrogation window of 1.25×1.25 mm^2 that is used for the PIV evaluation in the present study. The spatial averaging in the interrogation window results in a low-pass-filtered velocity signal. The transfer function can be expressed by a modified *sinc* function and the cutoff frequency depends mainly on the chosen interrogation-window size of 64 px $\times$ 64 px used in the study presented here [28]. The corresponding cutoff wave number is approximately 2.2 rad/mm based on a -3 dB attenuation in the spectrum. The dominant wave number can be estimated to be $k_d \approx 2\pi/(3.5d) \approx 0.12$ rad/mm for the flowfield investigated in the present study [29]. This implies that dominant flow structures are not filtered while the gradients can still be resolved [6]. According to Foucaut and Stanislas [6] the first derivative (and therewith the vorticity) has the same cutoff frequency when calculated with a second-order difference scheme.

For all PIV measurements presented here, the adjusted pulse separation time between the laser pulses results in a particle displacement at the freestream velocity of approximately 15 pixels. The conservative assumption of a subpixel accuracy of 0.1 pixels results in an uncertainty of $\pm 0.0067 U_\infty$ for the velocity measurement. A detailed analysis of the subpixel accuracy of PIV evaluations and derived quantities in general goes beyond the scope of the present paper and we refer to others for such investigations [4–6]. Please note that the calculation of the correlation coefficient between the near- and far-field data is the main objective. This operation works as a filter, reducing the uncorrelated noise.

B. Numerical Differentiation

All velocity data are postprocessed by means of cardinal cubic B-spline functions in order to smooth the measurement results and to calculate spatial gradients of first and second order. At the border of the PIV field of view and close to the surface of the rod and the airfoil as well as at outlier positions, artificially and unrealistically high gradient values can occur. Consequently, only data points where measurement data are available in the area of the B-spline convolution kernel are considered for the calculation of the results presented here.

C. Calculation of the Cross-Correlation Coefficient

For the calculation of the cross-correlation coefficient $R_{\psi,p}$, p is defined as the summed-up pressure signals from all microphones, delayed with $t_d = |\mathbf{x}_{le} - \mathbf{x}_m|/c_0$. Here, $\mathbf{x}_{le}$ and $\mathbf{x}_m$ are the coordinates of the airfoil leading edge (LE) in the PIV measurement plane and the microphones, respectively. The microphone signals are normalized to their respective rms values before the summation. The procedure is similar to the well-known delay and sum beamforming [30].

V. Results and Discussion

Unless otherwise specified, the following results have been obtained from the configuration with $U_\infty = 50$ m/s and $y_{\text{rod}}/c = 0.05$. The axes in the figures are scaled to the chord length c: x and y are local coordinates in the measurement plane with the origin at the cylinder axis for $y_{\text{rod}}/c = 0$. The x axis points in the mean flow direction. ROI D and ROI F include areas of missing vectors corresponding to shadow zones of the laser light sheet.

A. Flowfield

Following Williamson [31] the vortex shedding in the cylinder wake at the Reynolds number $R_d = 50,000$ is defined as the *shear layer transition regime*. Instability vortices appear in the shear layers and three-dimensional structures are expected to develop in this regime. A few examples of the instantaneous velocity fields are shown in Fig. 4. For the purpose of clarity, only every second vector is plotted. All quantities are made dimensionless using the cylinder diameter d and the freestream velocity U_∞. The fluctuating velocity fields together with the corresponding vorticity maps are given in Figs. 4a–4d for different regions of interest. In Fig. 4a the large-scale vortices can be seen to emanate from the upper and lower shear layers, from which they form a von Kármán vortex street in the wake of the cylinder with embedded small-scale turbulence. The structures become less periodic with increasing downstream distance from the rod; here, the location and the geometry of the large-scale vortices are hard to recognize in the region around the leading edge of the airfoil (Figs. 4c and 4c). Figure 4d depicts the flowfield in the region of the trailing edge of the airfoil. In this region the vortices are less organized and the start of the airfoil wake can be just discerned with the help of the ω_z of opposing sign emanating from the trailing edge. The observations are consistent with results obtained by Jacob et al. [11]. They concluded that the leading edge is the main aeroacoustic source region because of the strong vortex–airfoil interaction. Flow statistics for all regions of interest are depicted in Fig. 5. Results for

ROI F-E and ROI A–D are superimposed in the plots on the left and the right sides, respectively. The root-mean-square values of the corresponding velocity fluctuations u' and v' are σ_u and σ_v. It should be noted that the value range in the plots differs between the region around the rod and the airfoil LE region. In Fig. 5a strong u fluctuations can be observed in the shear layer where the formation of the vortices takes place. High values of σ_v can be identified in Fig. 5c in the near-wake region of the cylinder, reaching a maximum at approximately $1.6d$ downstream. Rapid acceleration of the released vortices takes place in this region. Because of the fact that the cylinder position has been shifted to $y_{\text{rod}}/c = 0.05$, the distribution of statistical quantities in Figs. 5b and 5d is asymmetric relative to the $y = 0$ axis. A spot of high σ_v values close to the airfoil LE in 5d corresponds to low σ_u values in 5b. Here, u' vanishes and its energy is transferred into the v' component [11].

B. Acoustic Results

Acoustic frequency spectra are calculated with a number of 600 averages using a Hanning window and a total averaging period of 120 s. The frequency resolution is 10 Hz. Sound pressure levels are given in decibels with a reference pressure of $p_{\text{ref}} = 2 \times 10^{-5}$ Pa. A set of spectra for different configurations with $U_\infty = 50$ m/s is depicted in Fig. 6a. The spectra for the rod-airfoil configuration for both y_{rod} positions as well as the frequency distribution for the noise generated by the rod and the flow only are plotted. The spectra indicate that the shift of the rod to $y_{\text{rod}}/c = +0.05$ causes an increase of the second harmonic, while the first harmonic is attenuated, but does not change the fundamental characteristics of the leading-edge interaction mechanism. Compared to the noise generated by the rod only, the sound level is about 10 dB higher when the airfoil is in its downstream position. 6b depicts the autocorrelation function of p'. It illustrates the strong coherence of the pressure fluctuations and therewith the need for a low sampling frequency in order to obtain statistically independent PIV snapshots. The results are obtained from a single-array microphone located at 90° to the flow direction at $x/c \approx 1$ in the coordinate system described in Fig. 2. The authors refer to Jacob et al. [11] for a detailed description of the spectra, sound levels, and directivity obtained from measurements on a similar flow configuration.

C. Cross-Correlation Results

Five thousand PIV snapshots are considered for the comparison of the cross-correlation results; this number corresponds to the maximum number available for all fields of view. Note that the final error margin for $R_{\psi,p}$ with 5000 samples is approximately ± 0.048 based on a t test against *zero* (99.9% probability). Figure 7 shows the instantaneous distribution of the cross-correlation coefficient $R_{\omega_z,p}$ at ROI A–F for $\tau = 0$ ms. p is the pressure fluctuation measured at all microphones delayed and summed up as described in Sec. II. The sign of $R_{\omega_z,p}$ alternates between positive and negative values downstream of the cylinder and becomes close to zero for regions outside of the cylinder wake. The increasing distance between two neighboring local maxima further downstream can be explained by the acceleration of the emanating vortices. In Fig. 8 $[R_{u,p}, R_{v,p}]$ is depicted as a vector field for ROI F and A. A regular pattern of vortical structures can be identified downstream of the rod. These vortical structures split at the leading edge and stretch along the airfoil. The resulting pattern has a strong similarity to the first POD modes, satisfactorily describing the vortex–airfoil interaction (see Jacob et al. [11] and references therein). Previous results have already indicated that the correlation technique functions as a filter of the most energetic structures in the flow, which are responsible for the sound generating process [10].

Note that the values of $R_{\omega_z,p}$ (Fig. 7) are maximal in the near-wake of the cylinder and not at the airfoil LE. This is remarkable, since the leading edge is suspected to be the main aeroacoustic source region. But the flow structures become less periodic with increasing downstream distance from the rod (see Fig. 4) and most likely more three-dimensional. Therefore, and because of the resulting higher noise level of v' and u' in the LE region, a lower correlation coefficient is observed in this area. It will be shown in the following that the temporal evolution of $R_{v,p}$ with τ supports this explanation; and that the main source region can indeed be attributed to the leading edge of the airfoil by means of the correlation technique presented here.

The temporal evolution of the cross-correlation coefficient $R_{v,p}$ at position $[x/c; y/c] = [0.16; 0.05]$ obtained from the measurement at the ROI F is plotted in Fig. 9a. The cross-correlation coefficient fluctuates over time in a sine-type oscillation with maximum values of about $|R_{v,p}| = 0.36$ (minima in the distribution of $R_{v,p}$). The

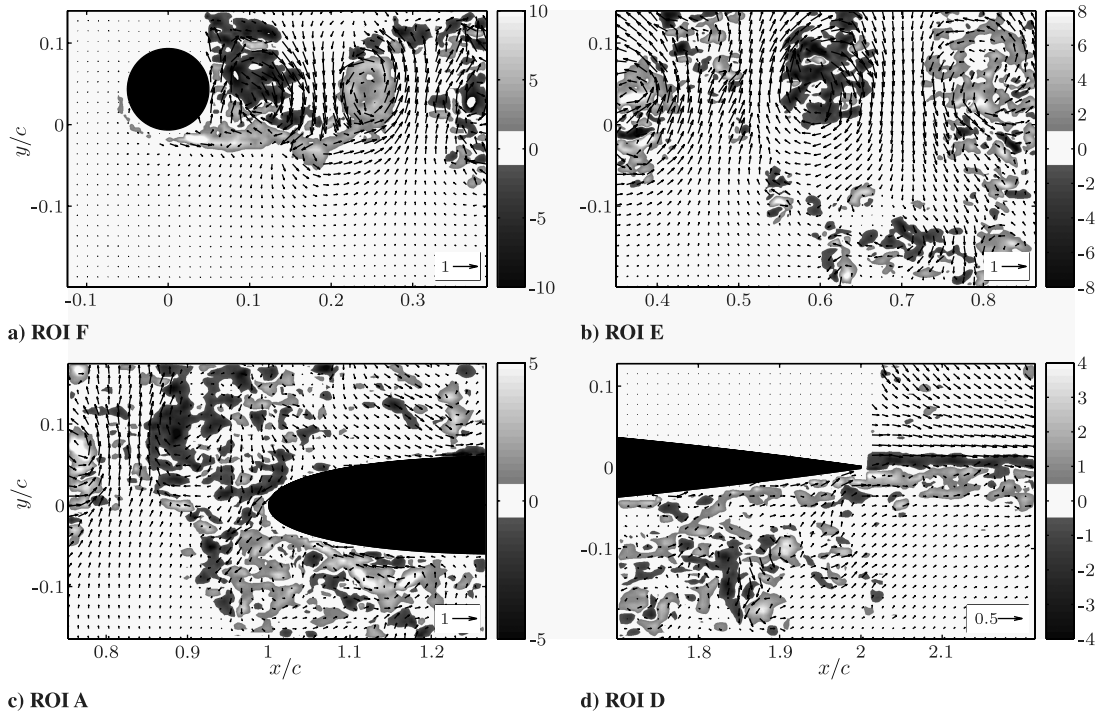

Fig. 4 Instantaneous velocity fields obtained from the PIV measurements for ROI F, E, A, and D. Local mean velocities $U(x,y)$ and $V(x,y)$ are subtracted. Reference vectors are given in the lower right corners. The normalized vorticity $\omega_z d/U_\infty$ is grayscale-coded in the background.

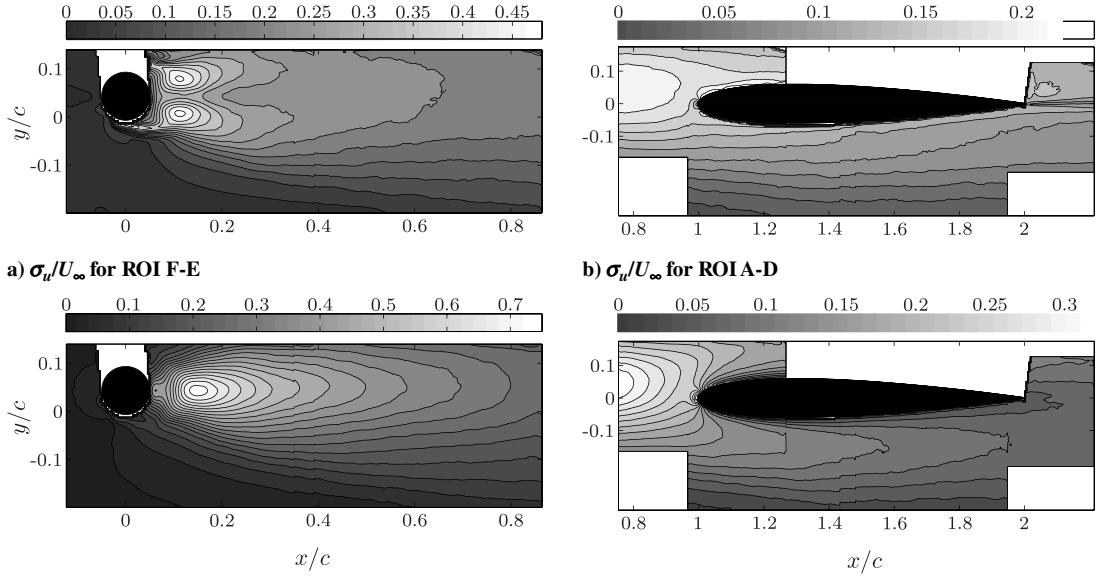

a) σ_u/U_∞ for ROI F-E

b) σ_u/U_∞ for ROI A-D

c) σ_v/U_∞ for ROI F-E

d) σ_v/U_∞ for ROI A-D

Fig. 5 Statistical flow quantities obtained from the PIV measurements for ROI F, E (top) and A–D (bottom).

envelope of $|R_{v,p}|$ as a function of τ shows almost no skewness and the distribution is symmetric around a maximum, located near $\tau = 0$ ms. This results differ significantly from findings in [10], where a similar experiment has been conducted in the near-wake of a rod installed in a closed test section with reverberant side walls. Therein the authors observed the correlation coefficient to be shifted toward larger τ values, not matching with the sound travel time directly from the cylinder to the installed inflow microphone. This difference in shape as well as the larger kurtosis of the envelope has been assigned to the dominance of the reflected waves from the side

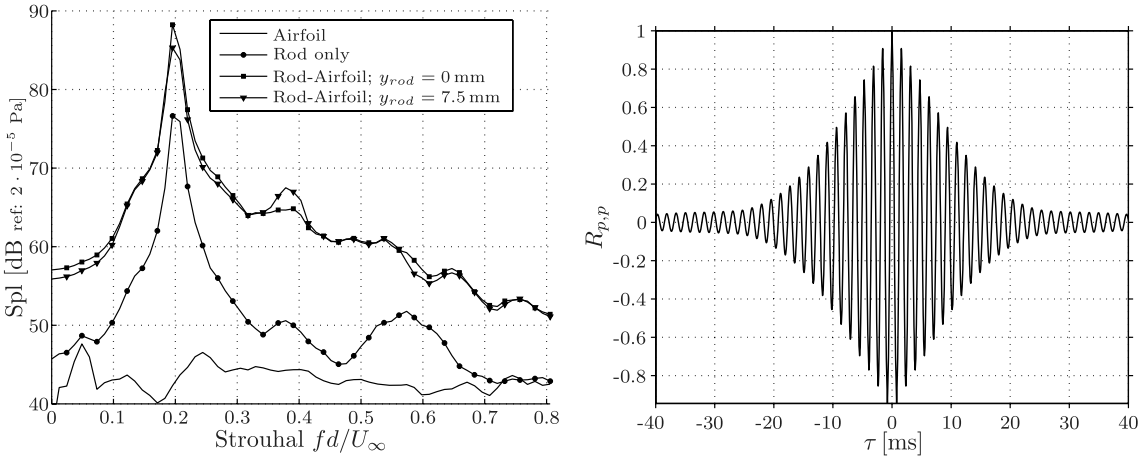

a) b)

Fig. 6 Plots of a) comparison of sound pressure levels for different configurations with $U_\infty = 50$ m/s and b) autocorrelation function of p' for the rod-airfoil configuration with $y_{rod}/c = +0.05$ and $U_\infty = 50$ m/s.

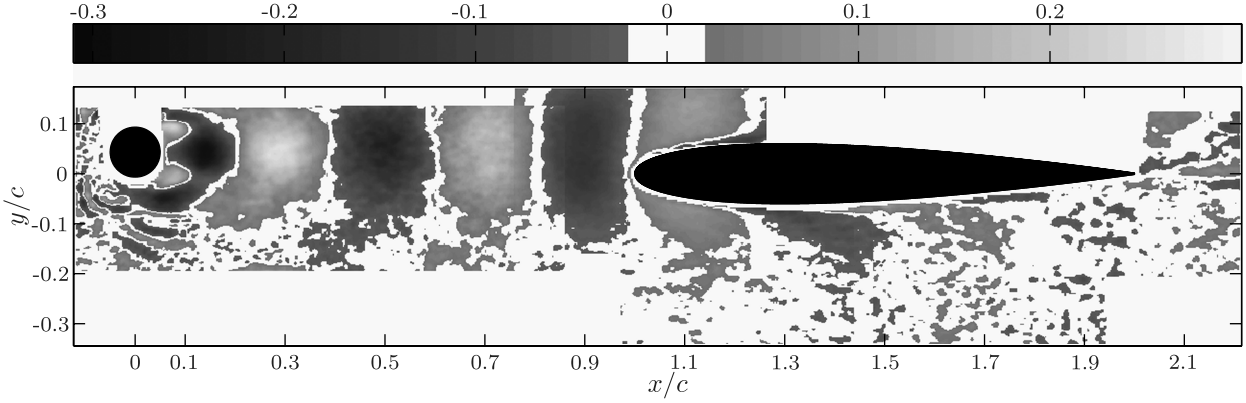

Fig. 7 Instantaneous distribution of $R_{\omega_z,p}$ for $\tau = 0$. The results for the ROI A–F are superimposed.

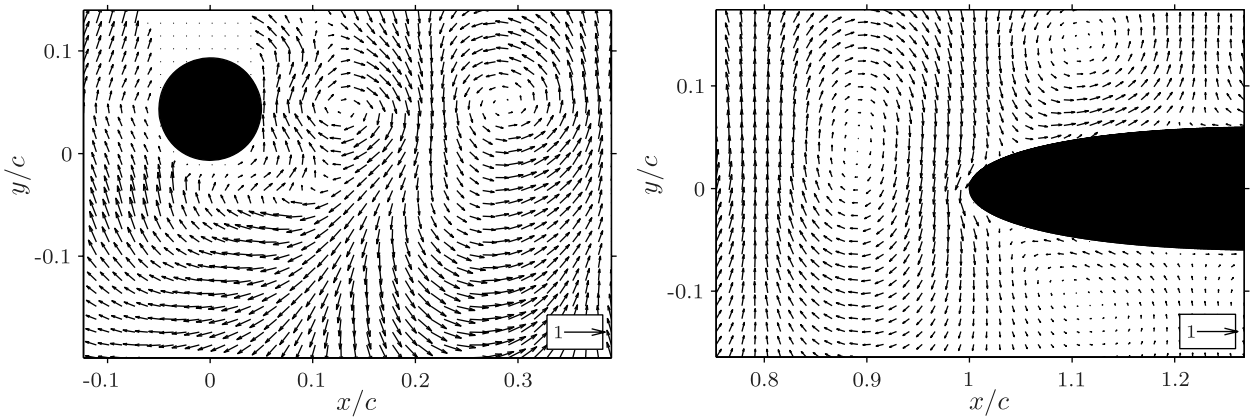

a) *ROI F* b) *ROI A*

Fig. 8 Instantaneous distribution of the cross-correlation coefficients ($R_{u,p}, R_{v,p}$) for $\tau = 0$ ms as a vector plot; ROI F in the region of the rod (left) and ROI A near the airfoil leading edge (right).

walls. This is not the case in the present investigation, where strong reflections are damped by the anechoic chamber.

The evolution of $R_{v,p}$ at position $[x/c; y/c] = [0.95; 0.00]$ obtained from the measurement at the ROI A is depicted in Fig. 9b. Major differences can be pointed out comparing this plot to Fig. 9a. The kurtosis of the envelope is smaller in the region of the airfoil LE compared to the one in the cylinder wake flowfield. $R_{v,p}$ is minimal at $\tau \approx 0$ ms in front of the airfoil LE. For the cylinder wake its minimum is located at approximately $\tau \approx 4$ ms. This shift cannot be attributed to the larger sound travel time from the cylinder to the microphones, since

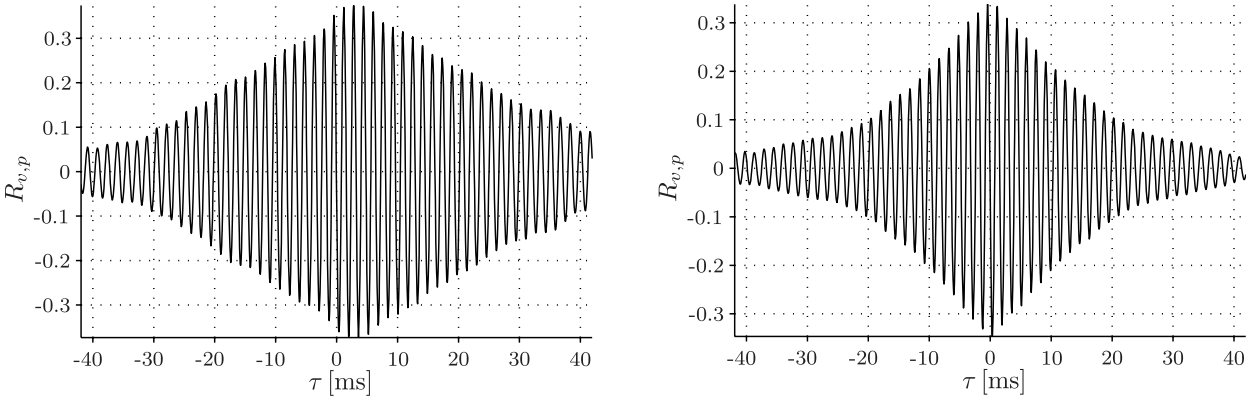

a) *ROI F* b) *ROI A*

Fig. 9 Temporal evolution of the cross-correlation coefficients ($R_{v,p}$) with τ: $[x/c; y/c] = [0.165; 0.05]$ near the cylinder wake (left) and $[x/c; y/c] = [0.95; 0]$ near the leading edge of the airfoil (right).

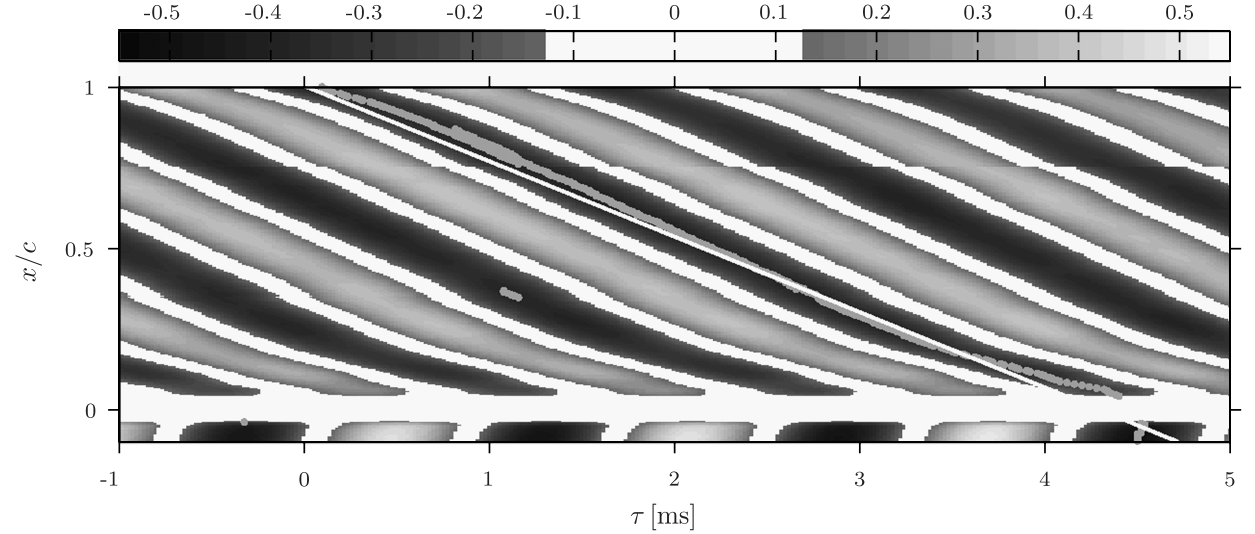

Fig. 10 Evolution of the correlation coefficient $R_{v,p}$ with τ and x along the axis $y = 0$. Maximum values along τ are marked by gray dots. The solid line depicts $\tau_c(x) = (c - x)/U_c$, with $U_c = 3.5\,\mathrm{St}\,U_\infty$.

the largest difference for an outer microphone would be of the order of 10^{-4} s. The evolution of the correlation coefficient $R_{v,p}$ with τ and x along the axis $y = 0$ is shown in Fig. 10. Minimum values $\min_\tau(R_{v,p}(x, \tau))$ along τ are marked by gray dots. The solid line depicts $\tau_c(x) = (c - x)/U_c$, with $U_c = 3.5\,\mathrm{St}\,U_\infty$ being the group velocity of the flow structures [29]. The phase shift of $R_{v,p}$ with an increasing upstream distance from the airfoil LE is indicated by the diagonal pattern in the distribution. The phase shift of the absolute minima in the positive τ direction corresponds to the group velocity $U_c = 3.5\,\mathrm{St}\,U_\infty$ of the flow structures traveling the distance $c = 0.15$ m between the rod and the airfoil. It is interesting that in the region upstream of the rod ($x/c < 0$) high values of $R_{v,p}$ can be observed. Here, the phase shift of $R_{v,p}$ with decreasing x does not correspond to a group velocity while the locations of minimum values are still shifted into the positive τ direction. It is assumed here that mainly harmonic oscillations are causing velocity fluctuations. These fluctuations are not superimposed by turbulent motions in the flow and exhibit a strong coherence with the fluctuations downstream of the rod. Therefore, values of $R_{v,p}$ are highest in this region. Now τ^* will be defined as the point in time at which $R_{v,p}(\mathbf{x}, \tau)$ is minimum with

$$R_{v,p}(\mathbf{x}, \tau^*) = \min_\tau(R_{v,p}(\mathbf{x}, \tau)) \tag{5}$$

Figure 11 shows the spatial distribution of τ^* for ROI A, E, and F. The shift in the positive τ direction with an increasing upstream distance from the airfoil LE is clearly visible in the whole investigated area. Note again that this shift cannot be attributed to the larger sound travel time from the cylinder to the microphones. Therefore, it can be concluded that the main source region can indeed be attributed to the leading edge of the airfoil by means of the correlation technique presented here.

D. Intensity Results

Figure 12a shows the results for the time-averaged intensity $[\langle I_x\rangle; \langle I_y\rangle]$ as a vector plot. $\mathbf{I}$ is calculated using Eq. (1) with $\phi = v$ as the acoustic variable. v is the y component normal to the mean flow direction. Here, 20,000 PIV snapshots are considered for the calculation. The vectors point to the airfoil LE, the region where v fluctuations are annihilated. Clearly, the sound intensity cannot be identified by this procedure because the resulting vector field is dominated by the main part of the convected turbulent structures.

A different approach will be tested in the following. Based on the concept presented here of correlating near-field quantities with the measured far-field pressure, $S_{\Psi,p}$ is calculated for the factors in Eq. (1). Then the resulting coefficients are multiplied:

$$\mathbf{I}_S = [+S_{v_x,p'} \times S_{v_t,p'}; +S_{v_y,p'} \times S_{v_t,p'}] \quad \text{with} \quad v_x = \frac{\partial v}{\partial x}$$
$$v_y = \frac{\partial v}{\partial y}, \qquad v_t = \frac{\partial v}{\partial t} \tag{6}$$

S is the cross-correlation function calculated using Eq. (3), and the resulting intensity $\mathbf{I}_S = [I_{Sx}; I_{Sy}]$ is a function of x, y, and the time-shift τ. The changed sign in Eq. (6) compared to Eq. (1) is due to the definition of τ in Eq. (3) being positive for a pressure signal occurring at a point in time after the PIV snapshot. The near-field intensity based on the correlation results is depicted as a vector plot $[I_{Sx}; I_{Sy}]$ for ROI A and $\tau = 0.16$ ms in Fig. 12b. The vectors show a wavelike

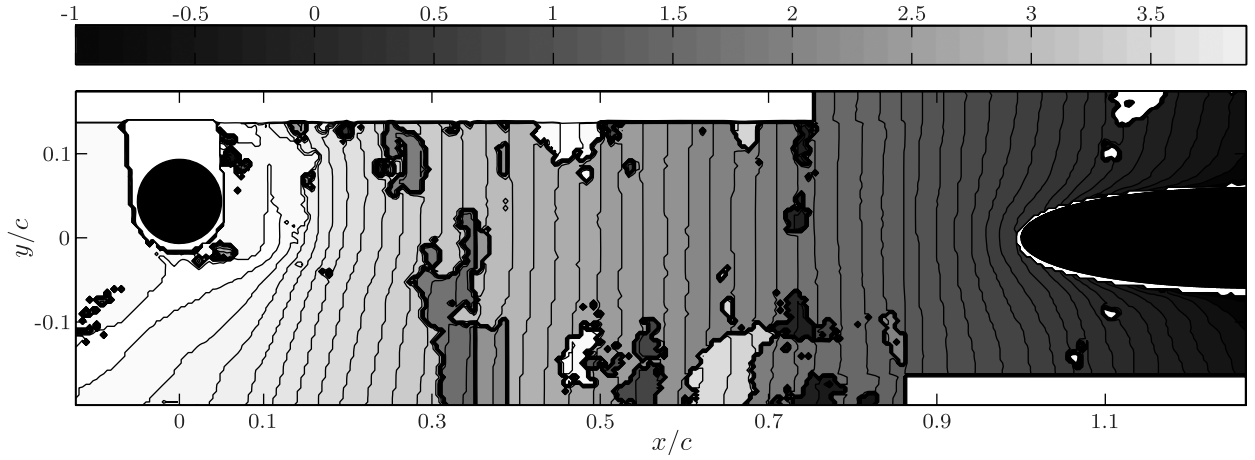

Fig. 11 Spatial distribution of τ^* in milliseconds [see Eq. (5)].

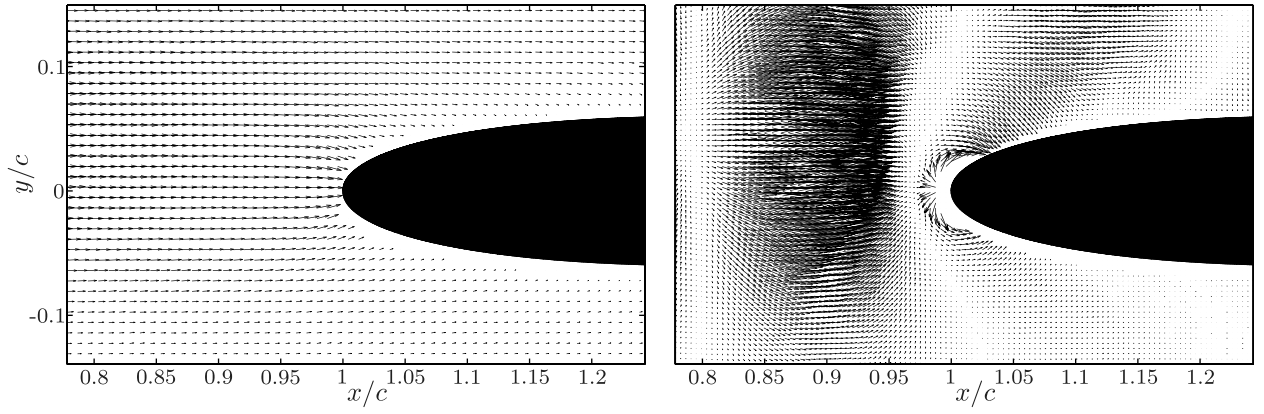

Fig. 12 Plots of a) time-averaged intensity $\langle \mathbf{I} \rangle$ calculated with v as the acoustic variable and b) near-field intensity based on the correlation results depicted as a vector plot $[I_{Sx}; I_{Sy}]$ for ROI A for $\tau = 0.16$.

pattern, mainly pointing in the downstream direction. It can be concluded that the intensity is dominated by convective effects and that the intensity contribution from the acoustic waves may be minuscule compared to the overall value. But for $\tau = 0.16$ ms some vectors near the leading edge of the airfoil are pointing outward. This can only be caused by compressibility effects. Thus, at least in the vicinity of the LE region, the fluctuating intensity (which is involved with the source process) becomes observable.

VI. Conclusions

The correlation technique presented here has been successfully applied to a rod-airfoil flow configuration. The large number of microphones results in a higher signal-to-noise ratio for the calculated cross-correlation coefficient, compared to the case when a single microphone is used for the correlation. Flow structures mainly describing the vortex–airfoil interaction, which are supposed to be the main sources of noise, are filtered out by the described method. It should be noted that the location of maximum values of $R_{\psi,p}$ alone cannot be interpreted as the origins of aeroacoustic sources. But by an analysis of the temporal evolution of $R_{\psi,p}$, the source region can be attributed to the leading edge of the airfoil.

Additionally, statistically independent samples of the temporal velocity derivatives are acquired and used for an intensity analysis with regard to an acoustic analogy.

Appendix: Cross-Correlation Using Differential Quantities

The temporal derivative v_t used in Eq. (6) can be determined using central differencing since the coplanar multiplane PIV system described in Sec. III.B captures the velocity fields at two successive time steps. If the time difference between these PIV snapshots is denoted by Δt, the cross-correlation $S_{v_t,p'}$ is calculated as

$$S_{v_t,p'}(\mathbf{x},\tau) = \left\langle \left(\frac{v(\mathbf{x},t) - v(\mathbf{x},t+\Delta t)}{\Delta t} \right) p'\left(t + \tfrac{1}{2}\Delta t + \tau \right) \right\rangle$$

with

$$\langle v(\mathbf{x}, t+\Delta t) p'(t) \rangle = \langle v(\mathbf{x}, t) p'(t-\Delta t) \rangle$$

After rearranging the terms, we get

$$S_{v_t,p'}(\mathbf{x},\tau) = \left\langle \left(\frac{v(\mathbf{x},t)}{\Delta t} \right) p'\left(t + \frac{1}{2}\Delta t + \tau \right) \right\rangle - \left\langle \left(\frac{v(\mathbf{x},t)}{\Delta t} \right) p'\left(t - \frac{1}{2}\Delta t + \tau \right) \right\rangle$$

This means that it is not necessary to measure the temporal velocity gradient directly if only its correlation with the far-field pressure fluctuation is investigated.

References

[1] Lighthill, M. J., "On Sound Generated Aerodynamically. Part I: General Theory," *Proceedings of the Royal Society of London A*, Vol. 211, 1952, pp. 564–587. doi:10.1098/rspa.1952.0060

[2] Lorenzoni, V., Moore, P., Scarano, F., and Tuinstra, M., "Aeroacoustic Analysis of a Rod-Airfoil Flow by Means of Time-Resolved PIV," 15th AIAA/CEAS Aeroacoustics Conference, Miami, FL, AIAA Paper 2009-3298, 2009.

[3] Crighton, D. G., "Computational Aeroacoustics for Low Mach Number Flows," *Computational Aeroacoustics*, edited by J. C. Hardin, and M. Y. Hussaini, Springer, New York, 1993, pp. 50–68.

[4] Westerweel, J., "Theoretical Analysis of the Measurement Precision in Particle Image Velocimetry," *Experiments in Fluids*, Vol. 29, 2000, pp. S003–S012. doi:10.1007/s003480070002

[5] Nobach, H., and Tropea, C., "Improvements to PIV Image Analysis by Recognizing the Velocity Gradients," *Experiments in Fluids*, Vol. 39, 2005, pp. 614–622. doi:10.1007/s00348-005-1001-9

[6] Foucaut, J. M., and Stanislas, M., "Some Considerations on the Accuracy and Frequency Response of Some Derivative Filters Applied to Particle Image Velocimetry Vector Fields," *Measurement Science and Technology*, Vol. 13, No. 7, 2002, pp. 1058–1071. doi:10.1088/0957-0233/13/7/313

[7] Clark, P. J. F., and Ribner, H. S., "Direct Correlation of Fluctuating Lift with Radiated Sound for an Airfoil in Turbulent Flows," *Journal of the Acoustical Society of America*, Vol. 46, No. 3, 1969, pp. 802–805. doi:10.1121/1.1911765

[8] Siddon, T. E., "Surface Dipol Strength by Cross-Correlation Method," *Journal of the Acoustical Society of America*, Vol. 53, No. 2, 1973, pp. 619–633. doi:10.1121/1.1913366

[9] Lee, H. K., and Ribner, H. S., "Direct Correlation of Noise and Flow of a Jet," *Journal of the Acoustical Society of America*, Vol. 52, No. 5, 1972, pp. 1280–1290. doi:10.1121/1.1913245

[10] Henning, A., Kaepernick, K., Ehrenfried, K., Koop, L., and Dillmann, A., "Investigation of Aeroacoustic Noise Generation by Simultaneous Particle Image Velocimetry and Microphone Measurement," *Experiments in Fluids*, Vol. 45, 2008, pp. 1073–1085. doi:10.1007/s00348-008-0528-y

[11] Jacob, M. C., Boudet, J., Casalino, D., and Michard, M., "A Rod-Airfoil Experiment as Benchmark for Broadband Noise Modeling," *Theoretical and Computational Fluid Dynamics*, Vol. 19, 2005, pp. 171–196. doi:10.1007/s00162-004-0108-6

[12] Jacob, M., Ciardi, M., Gamet, L., Greschner, B., Moon, Y., and Vallet, I., "Assessment of CFD Broadband Noise Predictions on a Rod-Airfoil Benchmark Computation," 14th AIAA/CEAS Aeroacoustics Conference, AIAA Paper 2008-2899, 2008.

[13] Greschner, B., Thiele, F., Casalino, D., and Jacob, M., "Prediction of Sound Generated by a Rod-Airfoil Configuration Using EASM DES and the Generalised Lighthill/FW-H Analogy," *Computers and Fluids*, Vol. 37, No. 4, 2008, pp. 402–413. doi:10.1016/j.compfluid.2007.02.013

[14] Möhring, "A Well Posed Acoustic Analogy Based on a Moving Acoustic Medium," *Aeroacoustic Workshop 1999*, edited by N. Koltzsch, and P. Kalitzin, Dresden, Germany, 1999, pp. 1–11.

[15] Howe, M. S., "Contributions to the Theory of Aerodynamic Sound, with Application to Excess Jet Noise and the Theory of the Flute," *Journal of Fluid Mechanics*, Vol. 71, Oct. 1975, pp. 625–673. doi:10.1017/S0022112075002777

[16] Adrian, R. J., "Particle-Imaging Techniques for Experimental Fluid Mechanics," *Annual Review of Fluid Mechanics*, Vol. 23, 1991, pp. 261–303. doi:10.1146/annurev.fl.23.010191.001401

[17] Adrian, R., "Dynamic Ranges of Velocity and Spatial Resolution of Particle Image Velocimetry," *Measurement Science and Technology*, Vol. 8, 1997, pp. 1393–1398. doi:10.1088/0957-0233/8/12/003

[18] Raffel, M., Willert, C. E., Wereley, S. T., and Kompenhans, J., *Particle Image Velocimetry—A Practical Guide*, 2nd ed., Springer, New York, 2007.

[19] Nobach, H., Damaschke, N., and Tropea, C., "High-Precision Sub-Pixel Interpolation in Particle Image Velocimetry Image Processing," *Experiments in Fluids*, Vol. 39, 2005, pp. 299–304. doi:10.1007/s00348-005-0999-z

[20] Kahler, C. J., "General Design and Operating Rules for Seeding Atomisers," 5th International Symposium on Particle Image Velocimetry, Busan, Korea, Paper 3207, Sept. 2003, .

[21] Henning, A., and Ehrenfried, K., "Frequency Resolution of High-Speed PIV," *8th ONERA-DLR Aerospace Symposium*, Gottingen, Germany, 17–19 Oct. 2007, pp. 1–12.

[22] Mei, R., "Velocity Fidelity of Flow Tracer Particles," *Experiments in Fluids*, Vol. 22, 1996, pp. 1–13. doi:10.1007/BF01893300

[23] Lauterbach, A., Ehrenfried, K., and Koop, L., "Procedure for the Accurate Phase Calibration of a Microphone Array," 15th AIAA/CEAS Aeroacoustics Conference, Miami, FL, AIAA Paper 2009-3122, 2009.

[24] Nobach, H., "Accuracy of Subpixel Interpolation in PIV and PTV Image Processing," Fachbereich Maschinenbau, Fachgebiet Stromungslehre und Aerodynamik, Technische Universität Darmstadt, Rept. 001/2004, Darmstadt, Germany, March 2004.

[25] Ronneberger, O., Raffel, M., and Kompenhans, J., "Advanced Evaluation Algorithms for Standard and Dual Plane Particle Image Velocimetry," *9th International Symposium on Application of Laser Technology to Fluid Mechanics*, Lisbon, Portugal, 1998, pp. 1–10, 10–1.

[26] Christensen, K., "The Influence of Peak-Locking Errors on Turbulence Statistics Computed from PIV Ensembles," *Experiments in Fluids*, Vol. 36, 2004, pp. 484–497. doi:10.1007/s00348-003-0754-2

[27] Santiago, J. G., Wereley, S. T., Meinhart, C. D., Beebe, D. J., and Adrian, R. J., "A Particle Image Velocimetry System for Microfluidics," *Experiments in Fluids*, Vol. 25, 1998, pp. 316–319. doi:10.1007/s003480050235

[28] Foucaut, J., Carlier, J., and Stanislas, M., "PIV Optimization for the Study of Turbulent Flow Using Spectral Analysis," *Measurement Science and Technology*, Vol. 15, 2004, pp. 1046–1058. doi:10.1088/0957-0233/15/6/003

[29] Howe, M., *Acoustics of Fluid-Structure Interactions*, Cambridge University Press, New York, 1998, Chap. 3.1.4, pp. 157–252.

[30] Mueller, T. J. (ed.), *Aeroacoustic Measurements*, Springer, New York, 2002.

[31] Williamson, C., "Vortex Dynamics in the Cylinder Wake," *Annual Review of Fluid Mechanics*, Vol. 28, 1996, pp. 477–539. doi:10.1146/annurev.fl.28.010196.002401

F. Coton
Associate Editor